

pubs.acs.org/JPCC Article

Graphene-Based Dual-Metal Sites for Oxygen Reduction Reaction: A Theoretical Study

Jiayi Xu,* Ayyappan Elangovan, Jun Li, and Bin Liu*



Cite This: J. Phys. Chem. C 2021, 125, 2334-2344



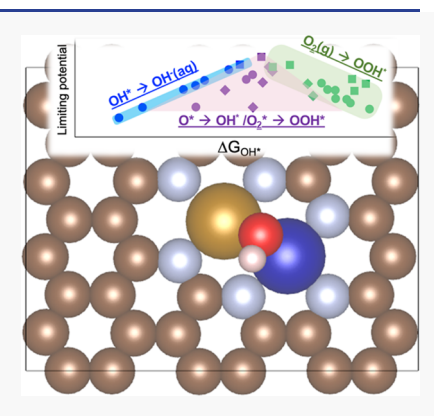
ACCESS

III Metrics & More

Article Recommendations

Supporting Information

ABSTRACT: Single-atom catalysts have expanded the design paradigm for oxygen reduction reaction (ORR) relying on nonplatinum group metals (non-PGM). Here, density functional theory calculations were performed on a variety of dual-metal active centers, consisting of both PGM (Pt and Pd) and non-PGM (Fe, Co, Ni, and Cu) metals, embedded in a monolayer of graphene and coordinated by six pyridinic nitrogen atoms. The dual-metal site stability, OH ligand effect, and electronic structures relevant to ORR were investigated. The ORR reactivities can be depicted in terms of a volcano diagram divided into multiple potential limiting regimes based on a wide range of $\Delta G_{\rm OH^*}$ values. In addition to OH removal and free molecular O_2 protonation as the potential-limiting steps, the protonation of adsorbed O_2 and O also emerge as likely potential-limiting steps due to strong O_2 adsorptions at certain dual-metal active sites. Among the systems investigated, Fe–Co(OH)_s exhibits the highest activity. Moreover, other PGM-free dual-metal sites such as Fe–Fe(OH), Fe–Cu(OH), and Co–Co(OH) also appear to be competitive and would encourage further explorations for Pt-free ORR electrocatalyst alternatives.



1. INTRODUCTION

Fuel cell technology is an essential toolset to mitigate our dependence on fossil-based fuels and to better engage with sustainable energy sources. ^{1–3} The efficiency of direct methanol fuel cells may reach up to 96.5%. ^{4,5} Currently, the choice for the electrocatalysts to carry out the cathodic oxygen reduction reaction (ORR) is primarily based on platinum group metals (PGMs); ^{6–8} however, the reliance on scarce catalytic materials poses severe limitation on achieving low-cost power generation (< \$30/kW) for wide-ranging applications. ⁹

Atomically dispersed transition metal single-atom catalysts (SACs), containing PGM or non-PGM active centers (e.g., Fe, Co, and Mn), offer an appealing solution by enabling competitive ORR pathways under both acidic and alkaline conditions. 9-16 For example, the single Pt atom active site coordinated by N dopants has a half-wave potential (one key metric for ORR activity) of 0.87 V in alkaline solutions (vs 0.84 V on standard bulk Pt catalysts). 17 Even higher ORR activities have been reported on non-PGM single-atom Fe species anchored in N-doped graphitic carbon, with a half-wave potential that is 30 mV higher than the standard Pt/C in alkaline solutions. 18 The X-ray absorption near-edge structure (XANES) confirmed that single-atom Fe active sites favor a FeN₄ configuration. ^{1,16,19–23} With the single-atom Fe attributed to the active site, a maximal atomic utilization for ORR can be ensured.

A broader group of N-doped SACs based on the metal-nitrogen-carbon (M-N-C) moieties are being discussed in the literature. These M-N-C moieties display a rich variety in their central metal ions and ligand

configurations. The ORR efficacy is also sensitive to the heteroatom codopants such as $B_{\nu}^{14}P_{\nu}^{26}$ and S^{13} or the presence of external ligands (e.g., OH, $^{24,27-30}$ O, 28 Cl, 31 NH₂, 32 and imidazole 33) directly associated with the active centers.

Dual-metal centers represent extended forms of SAC. 10 It has been reported that Fe dimers retain high ORR activity and could be even more stable than the single-atom FeN_x configuration.^{29,34} The investigation of ORR activity over a variety of dual-metal sites beyond Fe-Fe has also been carried out. Zinc-, 35-37 iron-, 38-42 or cobalt-36,37,40,43 containing dual-metal sites, paired with Ni, Cu, Pt, and Mn in characteristic MN₆ (see Figure 1) or MN₅-OH configurations, further enrich the repertoire of atomically dispersed electrocatalysts for ORR applications. On dual-metal sites, molecular O₂ binds frequently at the metal-metal bridge site. 26 The O-O bond cleavage is facilitated and proceed at lower energy barriers as the dissociated species may occupy different metal sites that function synergistically.³⁹ The measured ORR activity on the Pt-Co dual-metal site catalyst is 267 times higher than the bulk Pt catalyst. 43 The Fe-Co system is one remarkable dual-metal catalyst. The halfwave potentials obtained from the Fe-Co dual-metal system in respective acidic and alkaline solutions are 0.86 and 0.95 V,

Received: November 26, 2020 Revised: January 12, 2021 Published: January 26, 2021





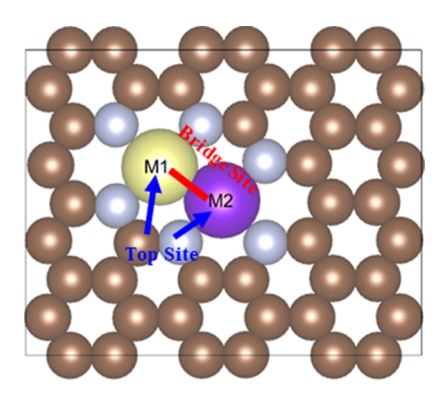


Figure 1. Molecular structure of the dual-metal active center anchored with six pyridinic nitrogen atoms in a periodic monolayer graphene sheet. Color scheme: brown-graphitic carbon, gray-pyridinic nitrogen, yellow-Metal site 1 (M1), and purple-Metal site 2 (M2).

versus 0.86 and 0.84 V on Pt/C under comparable conditions.^{39,44} The reported half-wave potentials for commercial Pt catalysts normally range from 0.8 to 0.9 V.^{39,45,46} Therefore, the Fe—Co dual-metal catalyst are quite attractive for large-scale ORR applications.

One of the restraints in M–N–C moiety design is that the active sites must withstand potential structural decay or decomposition under harsh ORR reduction potentials during long-term operations. Wang et al. demonstrated that the Fe–Co dual-metal cathode showed almost no voltage loss over a period of 100 h in the $HClO_4$ (0.1 M) solution. Zhang et al. dalso showed that the Fe–Co dual-metal site anchored in metal-organic frameworks exhibited negligible activity decay after 5000 voltage cycles in alkaline solutions (0.1 M KOH).

A number of theoretical dual-metal constructs have been proposed and investigated by Hunter et al. and Meng et al. 47,48 Here, we adopted a structure motif based on recent XANES and extended X-ray absorption fine structure analyses, which revealed that the Fe-Co dual-metal site is coordinated with six pyridinic N atoms in direct contact with the binuclear metal center (see Figure 1).^{39,44} Like single-metal sites (e.g., FeN₄), dual-metal configurations are also tunable through similar structure manipulation strategies. For instance, the potentiallimiting step (PLS) (e.g., OH removal) is mitigated by an external OH ligand due to the weakening of OH binding. 27,44 Density functional theory (DFT) calculations revealed that a weaker Fe-O bonding in FeCoN₅-OH leads to ORR activities surpassing that of FeN₄. 44 As reported by Holby and Taylor, 34 the limiting potential at the Fe-Co center with a bridging OH ligand coordinated by five pyridinic N at the graphene edge improves to 0.8 V.

To systematically survey the potential of dual-metal ORR electrocatalysts, periodic DFT was employed to investigate the impact of pairing in dual-metal sites that consist of Pt, Pd, Fe, Co, Ni, and Cu elements. In particular, the influence of the external OH ligand on the ORR rate-limiting step will be understood. The trends and behaviors will be revealed through electronic structure calculations and mechanistic analyses.

2. COMPUTATIONAL METHODS

Periodic, spin-polarized DFT calculations were performed using the plane-wave-based Vienna Ab initio Simulation Package (VASP). The projector augmented wave method was used to describe the wave functions of the ionic cores; the generalized gradient approximation PBE functional was used

to account for the electron exchange—correlation effects. ⁵² An energy cutoff of 520 eV was to determine the graphene (GN) lattice; then 440 eV was applied for regular geometry optimizations of O_2 , OOH, O_2 , and OH adsorptions at the dual-metal sites. The Monkhorst—Pack k-point mesh of $6\times6\times4$ was used for lattice optimization and $4\times4\times1$ was used for regular geometry optimizations, correspondingly. ⁵³ The convergence criterion for the self-consistent iteration was 1×10^{-6} eV; the ionic relaxations stopped when the force on each atom was less than 0.02 eV/Å. In this work, the Grimme's DFT-D3 theory was employed to account for the van der Waals interactions between adsorbates and substrates. ⁵⁴

As illustrated in Figure 1, the Fe–Co dual-metal site coordinated by 6 N atoms has been confirmed in nitrogendoped carbon structures. ^{39,44} Here, all dual-metal sites were constructed in a similar fashion. The relative stabilities of dual-metal active sites (denoted as M1–M2) were evaluated with the formation energy defined by eq 1, ⁵⁵ where the most stable crystal bulk of M1 and M2 elements, a pristine GN monolayer, and gas-phase N_2 were used as the reference state.

$$\Delta G_{\rm f} = E_{\rm dual-metal/GN} + 10\mu_{\rm C} - E_{\rm M1} - E_{\rm M2} - E_{\rm GN} - 3\mu_{\rm N_2}$$
(1)

In eq 1, $\mu_{\rm C}$ refers to the chemical potential of the carbon atom in a GN monolayer and its coefficient corresponds to the number of carbon atoms (10 atoms in total) removed to generate the vacancy to accommodate each dual-metal site. $E_{\rm M1}$ and $E_{\rm M2}$ are the total energies per atom in their respective bulk states. $E_{\rm dual-metal/GN}$ and $E_{\rm GN}$ represent the total energies of GN monolayer with and without the dual-metal site, respectively. Lastly, $\mu_{\rm N_2}$ represents the chemical potential of gas-phase N₂ at 1 atm and 298 K. All gas-phase species were modeled in a large vacuum box (20 × 20 × 20 ų).

The adsorption energies of O2*, OOH*, O*, and OH*, denoted as ΔG_{O2}^* ΔG_{OOH*} , ΔG_{O3}^* , and ΔG_{OH*} , were calculated based on eqs 2–5, using $\mu_{H,O}$ and μ_{H} , as references

$$\Delta G_{O_2^*} = G_{O_2^*} - E_* - 2(\mu_{H_2O} - \mu_{H_2}) - 4.92$$
 (2)

$$\Delta G_{\text{OOH}^*} = G_{\text{OOH}^*} - E_* - \left(2\mu_{\text{H}_2\text{O}} - \frac{3}{2}\mu_{\text{H}_2}\right)$$
(3)

$$\Delta G_{\text{O*}} = G_{\text{O*}} - E_* - (\mu_{\text{H,O}} - \mu_{\text{H,}}) \tag{4}$$

$$\Delta G_{\text{OH*}} = G_{\text{OH*}} - E_* - \left(\mu_{\text{H}_2\text{O}} - \frac{1}{2}\mu_{\text{H}_2}\right) \tag{5}$$

$$\Delta G = \Delta E + \Delta Z P E - T \Delta S + \Delta G_{IJ}$$
 (6)

Eq 6 was used to calculate the reaction free energy change for each elementary step, where ΔE represents the total energy change, and ΔZ PE and $T\Delta S$ represent the zero-point energy and entropy changes, respectively. For the former, we adopted ΔZ PE values reported by Nørskov and co-workers, i.e., 0.1, 0.4, 0.05, and 0.35 eV for O_2^* , OOH*, O*, and OH*, respectively. $^{35,56-58}$ $\Delta G_{\rm U}$ represents the energy contribution from the applied potential, -neU, where n is the number of electrons transferred in each elementary step, and U is the applied electrode potential. The solvation energies of the liquid-phase species, at 1 atm and room temperature, such as $H_2O(1)$ were obtained from the free energy differences between its gas and aqueous phase, according to ref 59.

$$O_2(g) + 2H_2O(1) + 4e^- \rightarrow 4OH^-(aq)$$
 (R1)

$$O_2(g) + * \rightarrow O_2^*$$
 (R2)

$$O_2^* + H_2O(l) + e^- \rightarrow OOH^* + OH^-(aq)$$
 (R3)

$$O_2(g) + H_2O(l) + e^- + * \rightarrow OOH^* + OH^-(aq)$$
 (R4)

$$OOH^* + e^- \rightarrow O^* + OH^-(aq)$$
 (R5)

$$O^* + H_2O(1) + e^- \rightarrow OH^* + OH^-(aq)$$
 (R6)

$$OH^* + e^- \rightarrow * + OH^-(aq)$$
 (R7)

In this paper, the ORR mechanism fitting for alkaline conditions is considered (R1). An outer-sphere electron transfer mechanism (as in R4) is frequently adopted if O2 adsorption on a crystalline catalyst surface is deemed weak. 46,60,51 However, for single-atom active centers, the molecular O2 adsorption state will play a more pronounced role in determining the rate-limiting potential. ^{60,62} Hence, the inner-sphere electron transfer mechanism (R2) will also be considered whenever $\Delta G_{O_{\bullet}^*} < 0$ 60,61 Following R2, the adsorbed O₂ is converted into OOH via a H₂O-coupled charge transfer step (R3), producing one OH⁻ ion. If $\Delta G_{O_2^*} > 0$, R4 will still be used as the initial ORR step. In this step, weak OOH binding typically indicates that subsequent O-O bond cleavage will likely be the PLS. After forming OOH* by accepting a second charge (R5), the O-O bond cleavage occurs forming O* and another OH⁻(aq). The O* species is then converted into OH* in a second H₂O-coupled charge transfer step (R6). Finally, OH* desorbs as an OH⁻ ion by accepting the fourth charge to vacate the active site (R7), which has been widely recognized as the PLS when OH binding becomes too strong, as on the Fe-Fe or Co-Co dual-metal sites.2

The limiting potential ($U_{\rm lim}$ in V), also referred as working potential ^{12,48,63} (or onset potential ^{47,64}), was employed to assess catalyst performance. Here, $U_{\rm lim}$ represents the largest free energy change among R3–R7^{14,35} and is expressed in eq 7.

$$U_{\text{lim}} = -\frac{\max[\Delta G_3, \Delta G_4, \Delta G_5, \Delta G_6, \Delta G_7]}{e}$$
(7)

3. RESULTS AND DISCUSSION

3.1. Stability of the Dual-Metal Configurations. The structural stability of M-N-C motifs depends on specific metal-metal and/or metal-ligand configurations. The metal-ligand interactions will be mainly governed by the M-N-type bonding (Figure 1). There is evidence showing that even with subtle variations, such as the coordination numbers associated with the M-N bonding and the separations between metal ions, the ORR performance will be impacted. 47,48

The formation energies $(\Delta G_{\rm f})$ for the illustrated dual-metal sites (Figure 1) are presented in Table 1. Holby et al. ⁴⁷ already showed that the FeN₄ site is less thermodynamically stable than the Fe–Fe dual-metal sites. According to eq 1, the lower formation energies indicate stronger cohesion for the overall system. The low $\Delta G_{\rm f}$ values obtained for both Fe–Fe and Fe–Co dual-metal sites are supported by prior studies in the literature. ^{27,42,47} For instance, the formation energy of Fe–Co is slightly lower than that of Fe–Fe, which is consistent with Yang et al. ²⁷ and Hunter et al. ⁴⁷ In an even broader context, the stability of Fe–Co under typical ORR conditions has been

Table 1. Adsorption Energies (in eV) of O_2 , OOH, O, and OH, the Dual-Metal Site Formation Energies (ΔG_f in eV), the Limiting Potentials (U_{lim} in V), and the corresponding PLS

	$\Delta G_{\mathrm{O}_2^*}$	$\Delta G_{ m OOH^*}$	ΔG_{O^*}	$\Delta G_{ ext{OH}^*}$	$\Delta G_{ m f}$	$U_{ m lim}$	PLS
Fe-Fe	-1.17	3.48	0.31	-0.13	4.07	-0.13	R7
Fe-Co	-0.94	3.96	0.46	0.35	4.00	0.02	R3
Fe-Ni	-0.62	3.97	0.77	0.34	3.92	0.33	R7
Fe-Cu	-0.94	3.70	1.00	0.27	4.24	0.27	R7
Co-Co	-1.05	1.94	0.48	0.02	4.40	0.02	R7
Co-Ni	-0.62	2.36	1.00	0.40	4.22	0.40	R7
Co-Cu	-0.31	4.12	1.54	0.70	4.34	0.48	R3
Ni-Ni	0.19	4.65	1.80	1.16	3.75	0.27	R4
Ni-Cu	0.21	4.66	2.24	1.21	4.12	0.26	R4
Cu-Cu	0.33	4.78	2.54	1.21	4.45	0.14	R4
Pt-Fe	-0.37	3.89	1.07	0.66	4.60	0.41	R6
Pt-Co	-0.27	3.98	1.14	0.55	4.98	0.55	R7
Pt-Ni	0.58	4.84	2.07	1.30	4.47	0.08	R4
Pt-Cu	0.61	4.93	2.64	1.42	4.64	-0.01	R4
Pd-Ni	0.34	4.79	2.12	1.28	4.46	0.13	R4
Pt-Pd	0.49	4.56	2.15	1.12	5.46	0.36	R4

extensively confirmed with both experimental and theoretical approaches in these studies. 39,44 Using the Fe–Co system as a benchmark, it can be learned that systems such as Fe–Ni, Fe–Cu, Co–Ni, and Ni–Cu also show comparable cohesive $\Delta G_{\rm f}$ values to Fe–Co. On the other hand, the Co–Co, Pt–Fe, Pt–Co, and Pt–Pd systems are not as stable. Such information can be used as metric, in additional to their intrinsic ORR reactivity, for the purpose of future catalyst screening.

3.2. ORR at Dual-Metal Sites. The preferred adsorptions of O_2 , OOH, O, and OH at the top or the bridge site are illustrated in Figures S1 and S2. Molecular O_2 can uniquely bind in di- σ , π , or η^1 configurations at these two-center dual-metal sites. The adsorption energies of O_2 will be used to determine the initial O_2 protonation in the $4e^-$ associative mechanism and are summarized in Table 1.

The hydroperoxyl (OOH) group always prefers the more oxophilic metal species at the dual-metal site, especially when a PGM atom (i.e., Pt or Pd) is paired with Fe, Co, or Ni. For Fe—Ni and Fe—Cu, OOH prefers the top sites of Fe. In Pt—Pd, where both atoms are PGM species, OOH prefers the Pd site. The optimizations of OOH at the Co—Co and Co—Ni sites resulted in O—O cleavage, and in this case, the coadsorptions of O and OH were considered instead. For the remaining dual-metal systems, their bridge or the tilted top site is preferred. As shown in Table 1, OOH binds the most strongly at the Fe—Fe site. The adsorption energy decreases for other Fe-containing heteronuclear dual-metal sites (i.e., one Fe is substituted by a different metal species). At Co—Cu, Ni—Ni, Ni—Cu, Cu—Cu, and the Pt(Pd)-containing dual-metal sites, the binding of OOH is much weaker.

The hydroxyl (OH) and atomic oxygen (O) always prefer the bridge site, but the calculated adsorption energies follow a similar pattern to OOH, that is, OH and O bind the most strongly at the Fe-Fe site, which is closely followed by Co-Co. The Ni-Cu, Cu-Cu, Pt-Cu, and Pd-Ni are among the weakest binding sites for OH and O.

Dual-metal centers support the 4e $^-$ ORR pathways, as represented by R1. ^{27,44,65} The free energy diagrams for the six dual-metal systems containing Pt or Pd are summarized in Figure 2 at three applied potentials. The profiles at 0 V are shown in blue and at their limiting potential ($U_{\rm lim}$) are shown in

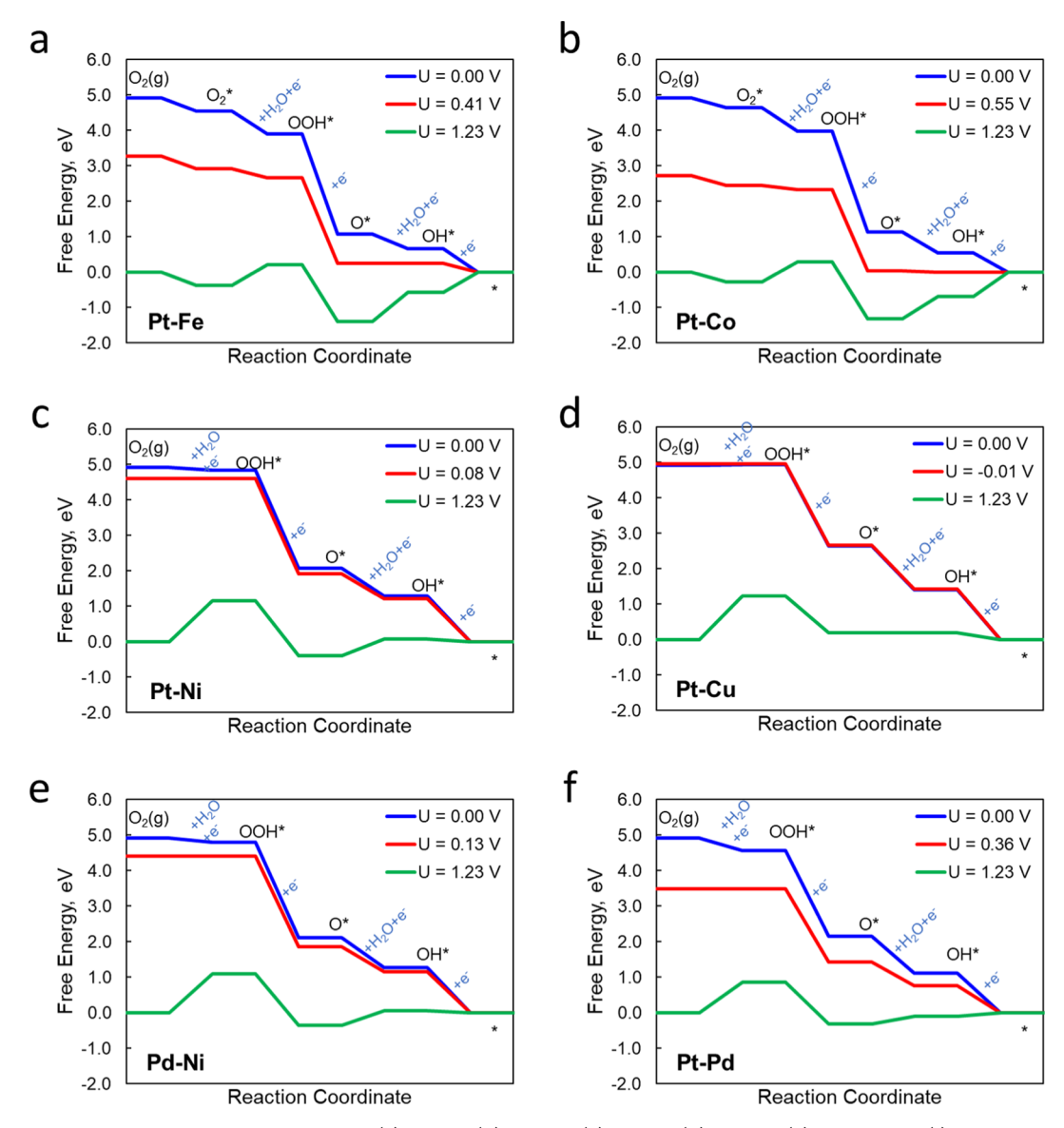


Figure 2. Free energy diagrams for six dual-metal sites: (a) Pt–Fe, (b) Pt–Co, (c) Pt–Ni, (d) Pt–Cu, (e) Pd–Ni, and (f) Pt–Pd, at U = 0 V (blue), U_{lim} (red), and U = 1.23 V (green). "*" indicates the clean surface.

red. Also, the free energy profiles obtained at $U=1.23~\rm V$ are shown in green. Based on $\Delta G_{O_2^*}$ listed in Table 1, ORR follows the outer-sphere electron transfer process (when $\Delta G_{O_2^*}>0$) except at the Pt–Fe and Pt–Co sites. For Pt–Fe (Figure 2a) and Pt–Co (Figure 2b), the PLSs corresponds to the conversions of O* into OH* at the active site (R6) and the removal of OH (R7), respectively. For Pt–Ni (Figure 2c), Pt–Cu (Figure 2d), Pd–Ni (Figure 2e), and Pt–Pd (Figure 2f), the protonation of gas-phase O_2 (R4) is the PLS, due to weak O_2 binding. For this group, the Pt–Co dual-metal site exhibits the highest limiting potential at 0.55 V.

The ORR free energy profiles representing the ten non-PGM dual-metal sites are summarized in Figure 3. On Fe–Fe (Figure 3a), O_2 , OOH, O_3 , and OH bind the strongest, and a negative U_{lim} (-0.13 V) is determined by the highly endothermic R7 step. At Fe–Co (Figure 3b) and Co–Cu (Figure 3g), U_{lim} is both determined by R3, involving the protonation of the adsorbed molecular O_2 . The removal of OH (R7) is the PLS for Fe–Ni (Figure 3c), Fe–Cu (Figure 3d), Co–Co (Figure 3e), and Co–Ni (Figure 3f). At the Ni–Ni (Figure 3h), Ni–Cu (Figure 3i),

and Cu–Cu (Figure 3j) sites, ORR follows the outer-sphere electron transfer process, and it was shown that the $U_{\rm lim}$ is determined by R4 (the protonation of gas-phase O_2). Overall, a trend characterizing the ORR mechanism at the PGM-free dualmetal sites emerges: with decreasing active-site oxophilicity, the PLS transition from the late-stage OH removal (R7), toward the protonation of adsorbed O (R6) and O_2 (R3), to the initial protonation of gas-phase O_2 (R4).

3.3. ORR at the Dual-Metal Sites Modified by OH Ligands. It has been shown that the strong binding OH at the Fe single-atom site also modulates the active-site electronic structures with implications to ORR performance. 10,24,27,28,30,34,44,66 As reported by Yang et al., 67 the OH ligand originates either from the ORR intermediate (in acidic environments) or directly from alkaline solutions. In this work, assuming alkaline conditions, an OH group was left at those dual-metal sites (with R7 as the PLS), which are denoted as M1–M2(OH). Subscripts 'o' and 's' are added to indicate ORR intermediates bind at the opposite or the same side of the preadsorbed OH ligand. The adsorption energies of ORR

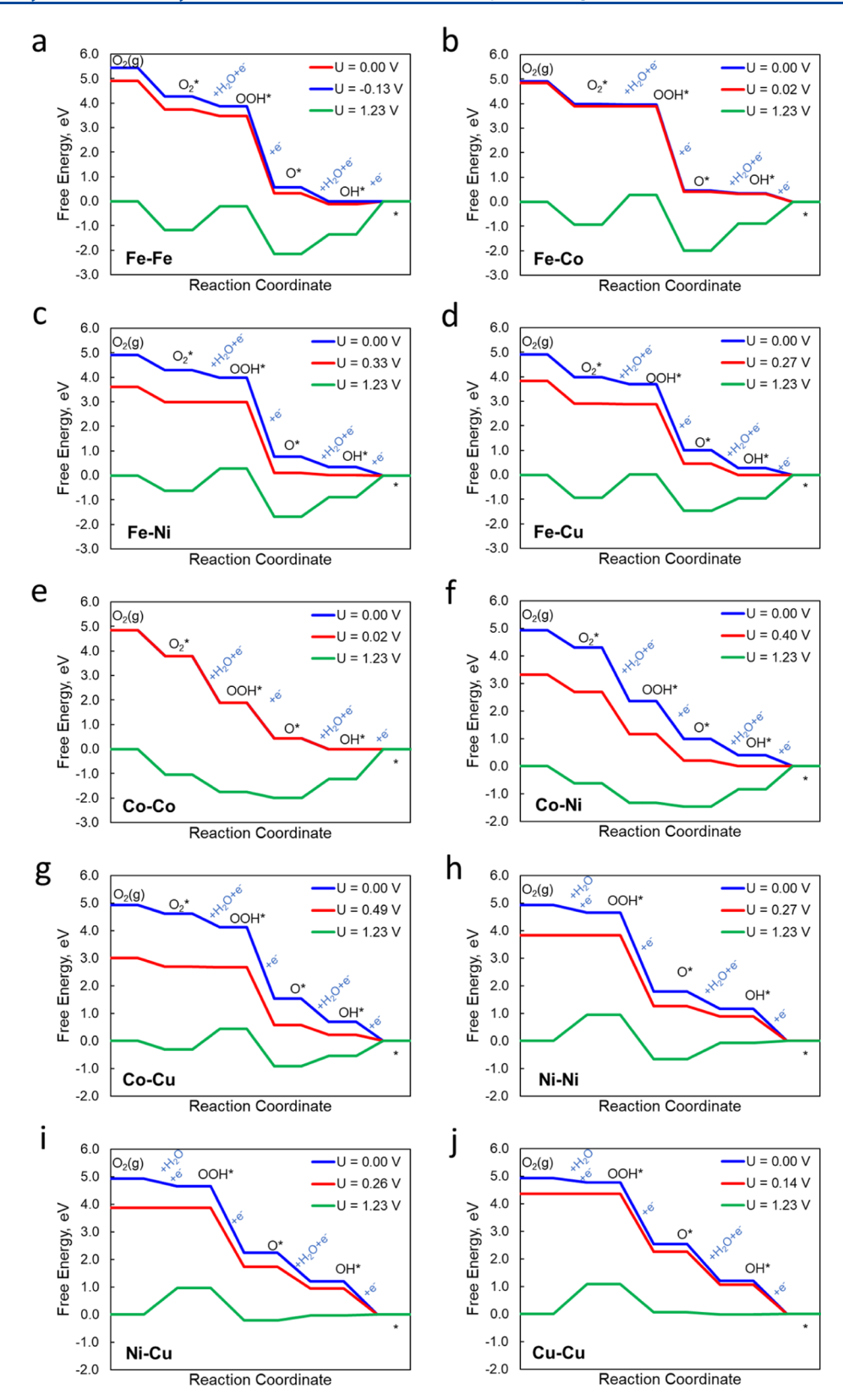


Figure 3. Free energy diagrams for ORR over PGM-free dual-metal sites: (a) Fe-Fe, (b) Fe-Co, (c) Fe-Ni, (d) Fe-Cu, (e) Co-Co, (f) Co-Ni, (g) Co-Cu, (h) Ni-Ni, (i) Ni-Cu, and (j) Cu-Cu, at U = 0 V (blue), U_{lim} (red), and U = 1.23 V (green). "*" indicates the clean surface.

intermediates at the modified M1–M2 dual-metal sites are shown in Table 2 (for M1–M2(OH) $_{\rm o}$) and S1 (for M1–M2(OH) $_{\rm s}$).

The top and side views of the optimized O_2 , OOH, O, and OH on M1-M2(OH)_o are illustrated in Figure S3. As shown in Table 2, the $\Delta G_{O_2^*}$ for all six dual-metal systems favors a molecular adsorption state, that is, $\Delta G_{O_2^*} < 0$, and were

Table 2. Adsorption Energies (in eV) of O_2 , OOH, O, and OH, Limiting Potentials (U_{lim} in V), and the Corresponding PLS for M1–M2(OH)₀.

	$\Delta G_{\mathrm{O}_2^*}$	$\Delta G_{ m OOH^*}$	ΔG_{O^*}	$\Delta G_{ ext{OH}^*}$	$U_{ m lim}$	PLS
Fe-Fe(OH) _o	-0.83	4.07	1.13	0.70	0.02	R3
Fe-Co(OH) _o	-0.76	3.90	1.19	0.53	0.26	R3
Fe-Ni(OH) _o	-0.44	4.11	1.52	0.76	0.37	R3
Fe-Cu(OH) _o	-0.16	4.17	1.88	0.80	0.59	R3
Co-Co(OH) _o	-0.32	4.42	2.14	1.07	0.18	R3
Co-Ni(OH) _o	-0.15	4.42	2.14	1.04	0.35	R3
$Pt-Co(OH)_{o}$	-0.24	4.15	2.27	0.82	0.53	R3

"Subscript "o" indicates that binding sites are on the opposite side of the OH ligand.

included in the ORR mechanism. Molecular O_2 prefers the bridge or the top site of the more oxophilic metal species in M1–M2(OH)_o.

The OOH species always prefer the top site of the more oxophilic metal species for M1-M2(OH)_o. As shown in Table 2, OOH binds the most strongly on Fe-Co(OH)_o, followed by Fe-Fe(OH)_o, Fe-Ni(OH)_o, Pt-Co(OH)_o, and Fe-Cu- $(OH)_o$. On Fe–Fe $(OH)_o$, Fe–Co $(OH)_o$, Fe–Ni $(OH)_o$, Co– $Co(OH)_{o}$, and $Co-Ni(OH)_{o}$, atomic O prefers the bridge site as a bridging oxygen, while on Fe-Cu(OH)_o and Pt-Co(OH)_o, O prefers the Fe (or Co) top site as an oxo-group (Figure S3). The O also binds the most strongly on Fe-Fe(OH)_o. For OH, the top sites of the more oxophilic metal atoms are preferred except for Fe-Fe(OH)_o (Figure S3). Just like OOH, OH binds most strongly on $Fe-Co(OH)_o$, followed by $Fe-Fe(OH)_o$, $Fe-Fe(OH)_o$ Ni(OH)_o, Fe-Cu(OH)_o, and Pt-Co(OH)_o. In fact, all ORR intermediates bind weaker than on ligand-free sites except for OOH at Fe-Co(OH)_o (Table 2). Particularly, ΔG_{OH*} universally shifts toward more positive values (i.e., weaker binding), compared with the bare dual-metal sites.

It has been previously shown that the single-atom Fe-N-C motifs modified by the S or P dopant in the π -bonded carbon supports exhibit enhanced ORR performance. 13,68 Functional groups with excess electrons in the proximity of the metal centers are shown to weaken the adsorbate binding by lowering the d-band center. Theoretically, the calculated net changes of the charges carried by the metal centers in all these systems change inversely with the adsorption energies of OH. 48,68 The Bader charge analysis was performed on all M1-M2(OH) systems and is presented in Figure S4. Figure 4 shows that with the nonparticipating OH ligand, charges are transferred away from the active sites (more positive Bader charge) when compared with the bare dual-metal centers. Furthermore, subsequent OH binding became weaker in the presence of an OH ligand. This observation further confirms that the electronwithdrawing effects as OH ligands shift the d-band centers downward.

Figure 5 summarizes the free energy diagrams for the ORR on M1–M2(OH) $_{\rm o}$. At U=0 V, the energy profiles of considered M1-M2(OH) $_{\rm o}$ systems show exothermic behaviors. According to the respective limiting potentials (red), the OH ligand shifts the PLS from R7 to R3. The $U_{\rm lim}$ associated with Fe–Fe(OH) $_{\rm o}$ (Figure 5a) has increased substantially to 0.02 V. In fact, all the variations in calculated $U_{\rm lim}$ indicate that the OH ligand plays an active role in facilitating OH desorption to varied extents. The $U_{\rm lim}$ values for Fe–Co(OH) $_{\rm o}$ (Figure 5b), Fe–Ni(OH) $_{\rm o}$ (Figure 5c), Fe–Cu(OH) $_{\rm o}$ (Figure 5d), and Co–Co(OH) $_{\rm o}$ (Figure 5e) have all increased, from 0.02, 0.33, 0.27, and 0.02 to 0.26, 0.37,

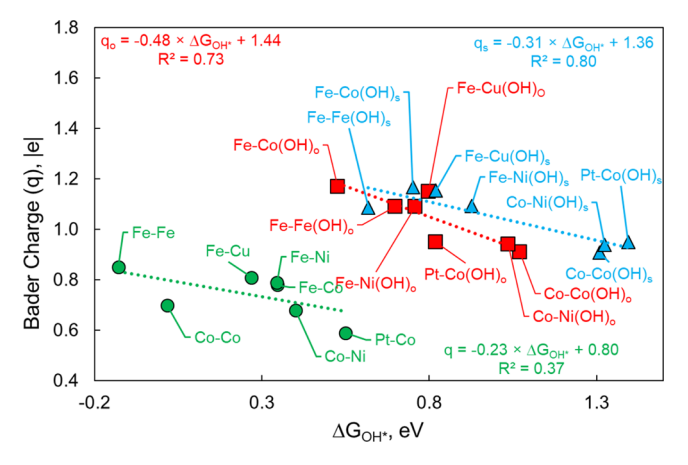


Figure 4. Relationship between ΔG_{OH^*} (eV) and the Bader charge (q, in |e|) at the OH binding site. The colored lines are used to guide the trend. Green indicates the relationship for the dual-metal sites without OH ligands, blue indicates the relationship on the same side with the OH ligand, and red indicates the relationship on the opposite sides of the OH ligand.

0.59, and 0.18 V, respectively. The enhancement on ORR activity at these dual-metal sites associated with the OH ligand is consistent with the observations reported in recent literature. ^{24,28,30,34,44,66} However, for Co–Ni(OH)_o and Pt–Co-(OH)_o, the presence of a OH ligand weakens OOH binding and will thus hinder ORR. Not surprisingly, the limiting potentials decrease from 0.40 to 0.35 V and from 0.55 to 0.53 V correspondingly.

Adsorptions of O_2 , OOH, O, and OH on $M1-M2(OH)_s$ were also considered and are shown in Figure S5, and the adsorption energies are summarized in Table S1. Unlike the bare and $M1-M2(OH)_o$ systems, the OH ligand at the bridge site will potentially block the access of other intermediates to this site as their first choice. Geometry optimizations showed that O_2 , OOH, O, and OH all will bind at the top sites of the oxophilic metal species. In general, the adsorptions of ORR intermediates are further weakened. This consequence reflects that ORR now follows an inner-sphere electron transfer process that is only applicable for Fe-Fe(OH)_s and Fe-Co(OH)_s.

The free energy profiles are summarized in Figure S6. The $U_{\rm lim}$ for Fe–Fe(OH)_s is still determined by the OH removal step (R7), while the PLS for the remaining M1–M2(OH)_s is the protonation of gas-phase O₂, forming OOH (R4). The highest $U_{\rm lim}$ was obtained from Fe–Fe(OH)_s, Fe–Co(OH)_s, Fe–Ni(OH)_s, and Fe–Cu(OH)_s, at 0.62, 0.73, 0.62, and 0.59 V, respectively. However, at the Co–Ni(OH)_s and Pt–Co(OH)_s sites, as shown in Figure S6 f and g, $U_{\rm lim}$ lower than that of the bare Co–Ni and Pt–Co sites was obtained due to weakened OOH binding.

Previous studies have established linear correlations among ORR intermediates for the purpose of ORR catalyst screening. 48,69,70 In this study, similar linear correlations were observed for O ($\Delta G_{\rm O*}$) and OOH ($\Delta G_{\rm OOH*}$) (Figure 6a), as well as molecular O₂ ($\Delta G_{\rm O_2*}$) (Figure S7) against $\Delta G_{\rm OH*}$ on the dualmetal sites with and without the OH ligand. The slope for the correlation between OH and O (1.62, see Figure 6a) is in a good agreement with the value (1.49) reported by Meng and coworkers. The slope for the correlation between OH and OOH is 0.92 (also see Figure 6a), which is also consistent extensively with previous reports (i.e., ~1). $^{48,70-73}$ Most notably, a decent correlation, with a slope of 1.11 ($R^2=0.84$), between OH and

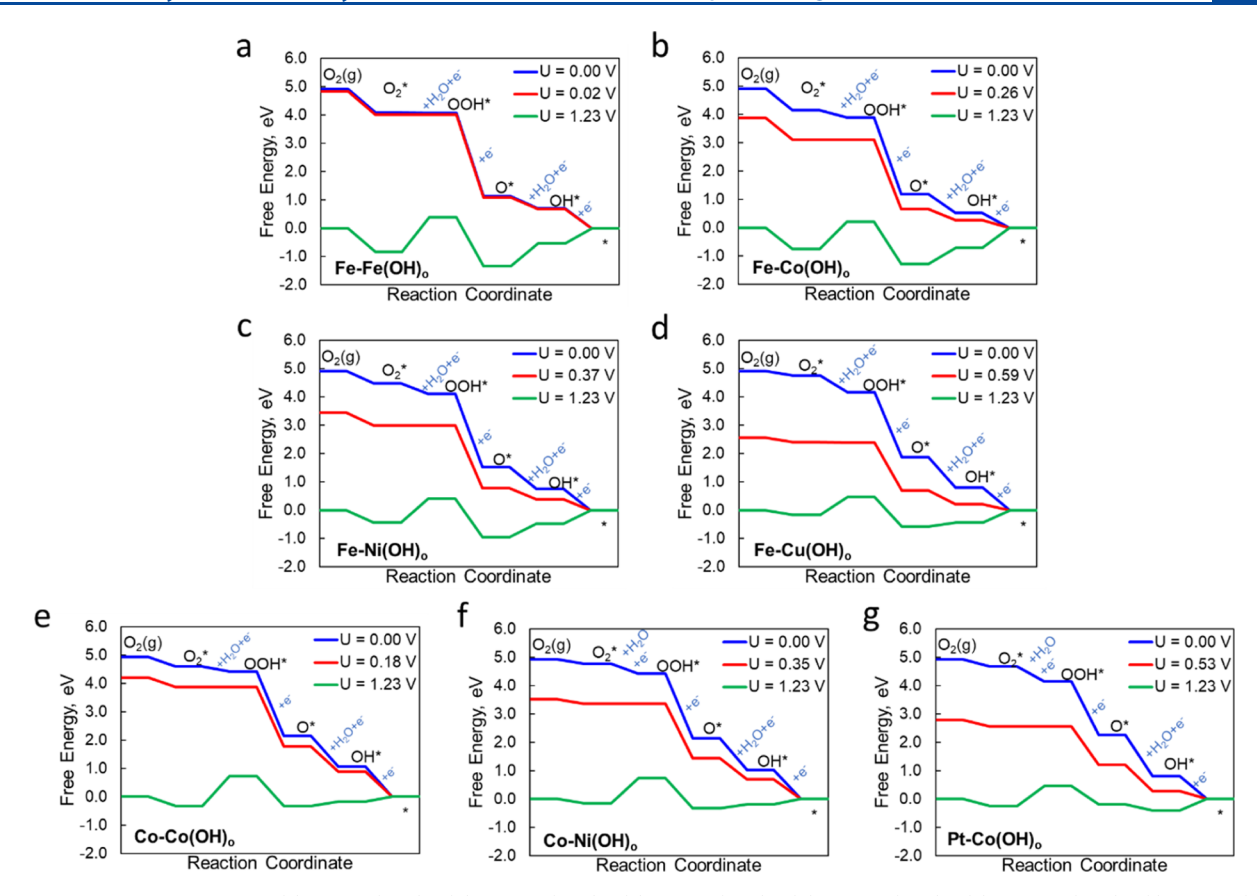


Figure 5. Free energy diagrams for (a) Fe–Fe(OH) $_{o'}$ (b) Fe–Co(OH) $_{o'}$ (c) Fe–Ni(OH) $_{o'}$ (d) Fe–Cu(OH) $_{o'}$ (e) Co–Co(OH) $_{o'}$ (f) Co–Ni(OH) $_{o'}$ and (g) Pt–Co(OH) $_{o}$ at U = 0 V (blue), U_{lim} (red), and U = 1.23 V (green). "*" indicates the clean surface. The subscript 'o' indicates that ORR happens at the opposite side of the OH ligand.

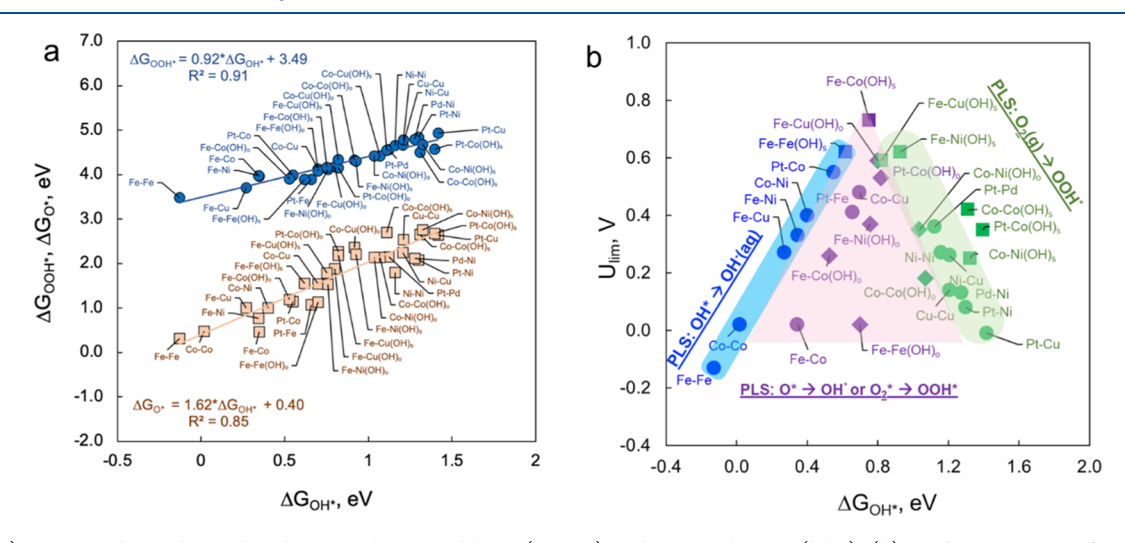


Figure 6. (a) Linear scaling relationships between $\Delta G_{\rm OH}$ and $\Delta G_{\rm O}$ (orange) and $G_{\rm OH}$ and $G_{\rm OOH}$ (blue). (b) Predicted $U_{\rm lim}$ as a function of $G_{\rm OH}$. Systems associated with the PLS (PLS) OH* \rightarrow OH_(aq)⁻ (left side) are colored in blue; systems associated with the PLS O* \rightarrow OH*_(aq) or O* \rightarrow OOH* (middle) are colored in purple; and system associated with the PLS O_{2(g)} \rightarrow OOH* (right side) are colored in green. In addition, the bare dual-metal centers are represented in dots, the dual-metal centers with ORR occurring on the same side with the OH ligand are represented by squares, and the dual-metal centers with ORR occurring on the opposite side of the OH ligand are represented by diamonds.

the adsorbed O_2 was also established, as shown in Figure S7. A rather broad range of $\Delta G_{O_2^*}$ values (-1.2-0.5 eV) was observed, indicating that the binding of molecular O_2 is sensitive to the compositions of the dual-metal sites. For systems such as Fe–Fe and Co–Co, the stable O_2 adsorption state (without O–O bond cleavage) may not be completely neglected.

When the $U_{\rm lim}$ for all dual-metal systems is organized based on $\Delta G_{\rm OH^*}$ (Figure 6b), $U_{\rm lim}$ peaks at a $\Delta G_{\rm OH^*}$ value of approximately 0.8 V. Moreover, the dual-metal systems included in this volcano-like trend can be generally grouped in three regimes following the identified PLS: (I) strong OH binding dual-metal sites with R7 as the PLS, (II) intermediate OH binding dual-metal sites with R3 or R6 as the PLS, and (III)

weak OH binding dual-metal sites with R4 as the PLS. The dualmetal sites in regime I (blue) form a strictly linear left boundary, as shown in Figure 6b. In this case, $U_{\rm lim}$ is purely dictated by $\Delta G_{\mathrm{OH}*}$, which is also used as the ORR performance descriptor. Almost all the dual-metal systems in this regime are OH-ligandfree (represented by dots) except for Fe-Fe(OH)_s. It is also evident that all these dual-metal sites contain at least one Fe or Co, which are both strong OH binding species. On the other hand, the right boundary formed by the dual-metal sites from regime III (green) is more scattered, governed by $\Delta G_{O_3^*}$ instead. Hence, the less-define nature reflects the correlation between ΔG_{OH^*} and $\Delta G_{\text{O}_2^*}$ (Figure S7). By inspection, common elemental species in these dual-metal sites are Pt, Pd, Cu, and Ni, occasionally coupled with Fe and Co. When Fe or Co is present, the dual-metal site always contains the OH ligand, as M1-M2(OH)_s (square). In this case, as discussed previously, the OH ligand tends to weaken the bindings of O2, O, OH, and OOH much more effectively. The ORR performance in the dual-metal systems in regimes I and III is governed by one of the two conventional mechanisms, that is, either the strong OH binding (left leg) or the protonation of the free O₂ molecule (right leg). 35,47,48,69,70

In Figure 6b, we also identified several dual-metal systems (highlighted in purple) located in regime II. These diverse groups contain bare dual-metal sites (dots), such as Fe–Co, Pt–Fe, and Co–Cu; the same-side OH ligand (squares) such as Fe–Co(OH) $_{\rm s}$; and opposite-side OH ligands (diamonds) such as Fe–Fe(OH) $_{\rm o}$, Fe–Co(OH) $_{\rm o}$, Fe–Ni(OH) $_{\rm o}$, and Pt–Co-(OH) $_{\rm o}$. In this regime, corresponding to the intermediate $\Delta G_{\rm OH}{}^{*}$, the PLS that determines $U_{\rm lim}$ is the protonation of either O or O2 adsorbed at the dual-metal sites.

Overall, the mechanistic study based on DFT suggests that dual-metal compositions, ligands, and locations of ORR allow molecular O_2 adsorption to play an influential role and to subsequently alter the potential limiting step. Ramaswamy⁶⁰ has also recognized the necessity to consider O_2 adsorption at SAC sites in their respective investigations. In our final analysis, we tracked the variations of $U_{\rm lim}$ for the Fe–Co system to further elucidate the impact from the OH ligand. Interestingly, all three Fe–Co, Fe–Co(OH)_o, and Fe–Co(OH)_s systems are located in regime II. Also, the Fe–Co dual-metal site has already been reported for its promising ORR reactivity in a number of literature studies. ^{27,39,44,47,48} Without explicitly considering molecular O_2 adsorption at the Fe–Co site, the ORR has been suggested to be hindered by the difficulty in OH removal (i.e., R7). ^{27,31,47}

Molecular O_2 has a stable adsorption state on bare Fe–Co with a $\Delta G_{O_2^*}$ of -0.94 eV. The associated $U_{\rm lim}$ is 0.02 V (lower purple region in Figure 6b) with the protonation of adsorbed O_2 (R3) as the PLS. In Fe–Co(OH)_o, $\Delta G_{\rm OH^*}$ becomes more positive. Nevertheless, the PLS remains the same despite a small shift toward right, but $U_{\rm lim}$ increases above 0.2 V. In Fe–Co(OH)_s, $\Delta G_{\rm OH^*}$ continues to shift right (even more positive). At this point, the $U_{\rm lim}$ increases significantly to 0.73 V. This value matches the results predicted by Wang and co-workers. Moreover, other PGM-free dual-metal sites, such as Fe–Fe, Co–Co, and Fe–Cu, also exhibit enhanced ORR activities by the OH ligand. By comparing with the FeN₄ motif, which yields the limiting potential as 0.46 V, the dual-metal centers indeed display improved performance. The outstanding ORR activity of Fe–Co(OH)_s shows good consistency with Wang's

work.^{39,44} It is very encouraging to note that PGM-free catalysts are capable of replacing PGM-based ORR catalysts.

4. CONCLUSIONS

DFT calculations were performed on a variety of dual-metal active centers coordinated by six pyridinic nitrogen embedded in GN monolayer for 4e ORR. Both PGM (Pt and Pd) and non-PGM (Fe, Co, Ni, and Cu) metal species were considered. Moreover, the OH group was deliberately considered as a modulating ligand for the charge redistribution at the dual-metal sites that naturally bind OH strongly. The ORR reactivities at these dual-metal sites can be depicted in terms of a volcano diagram divided distinctively by multiple PLSs. Specifically, the traditional OH removal and the protonation of gas-phase O2 remain as the two boundaries for the ORR reactivity volcano when too strong or weak OH binding occurs at the active sites, respectively. However, due to the strong molecular O₂ adsorption at the dual-metal sites, protonation of adsorbed O₂ and protonation of O species also emerge as likely PLSs and thus enrich the electrochemistry for ORR. Among all dual-metal sites, Fe-Co(OH)_s is predicted to have the highest limiting potential, with a U_{lim} of 0.73 V, which remains consistent with literature findings. Also, the PGM-free dual-metal sites such as Fe-Fe(OH), Fe-Cu(OH), and Co-Co(OH) also appear to be competitive, which encourage further explorations for Pt-free ORR electrocatalysts.

ASSOCIATED CONTENT

Supporting Information

The Supporting Information is available free of charge at https://pubs.acs.org/doi/10.1021/acs.jpcc.0c10617.

Coordinates of optimized structures in VASP format (ZIP)

Molecular structures of ORR intermediates, Bader charge analysis, additional free energy diagrams, binding energies of ORR intermediates in M1-M2(OH)_s systems, and the correlation between ΔG_{OH^*} and $\Delta G_{\text{O}_3^*}$ (PDF)

AUTHOR INFORMATION

Corresponding Authors

Jiayi Xu – Tim Taylor Department of Chemical Engineering, Kansas State University, Manhattan, Kansas 66506, United States; orcid.org/0000-0003-1763-6251;

Email: jasonxjy@ksu.edu

Bin Liu — Tim Taylor Department of Chemical Engineering, Kansas State University, Manhattan, Kansas 66506, United States; orcid.org/0000-0001-7890-7612; Email: binliu@ksu.edu

Authors

Ayyappan Elangovan – Department of Chemistry, Kansas State University, Manhattan, Kansas 66506, United States; orcid.org/0000-0002-0985-2475

Jun Li – Department of Chemistry, Kansas State University, Manhattan, Kansas 66506, United States; [™] orcid.org/ 0000-0002-3689-8946

Complete contact information is available at: https://pubs.acs.org/10.1021/acs.jpcc.0c10617

Notes

The authors declare no competing financial interest.

ACKNOWLEDGMENTS

The authors thank the National Science Foundation (CBET-1703263) for financial support. The authors are also grateful for the supercomputing support from the Beocat Research Cluster at Kansas State University, funded in part by NSF grants CHE-1726332, CNS-1006860, EPS-1006860, and EPS-0919443 and the National Energy Research Scientific Computing Center (NERSC) under the contract no. DE-AC0205CH11231.

REFERENCES

- (1) Lefèvre, M.; Proietti, E.; Jaouen, F.; Dodelet, J.-P. Iron-Based Catalysts with Improved Oxygen Reduction Activity in Polymer Electrolyte Fuel Cells. *Science* **2009**, 324, 71–74.
- (2) Debe, M. K. Electrocatalyst Approaches and Challenges for Automotive Fuel Cells. *Nature* **2012**, *486*, 43–51.
- (3) Staffell, I.; Scamman, D.; Velazquez Abad, A.; Balcombe, P.; Dodds, P. E.; Ekins, P.; Shah, N.; Ward, K. R. The Role of Hydrogen and Fuel Cells in the Global Energy System. *Energy Environ. Sci.* **2019**, 12, 463–491.
- (4) Tiwari, J. N.; Tiwari, R. N.; Singh, G.; Kim, K. S. Recent Progress in the Development of Anode and Cathode Catalysts for Direct Methanol Fuel Cells. *Nano Energy* **2013**, *2*, 553–578.
- (5) Zou, L.; Fan, J.; Zhou, Y.; Wang, C.; Li, J.; Zou, Z.; Yang, H. Conversion of PtNi Alloy from Disordered to Ordered for Enhanced Activity and Durability in Methanol-Tolerant Oxygen Reduction Reactions. *Nano Res.* **2015**, *8*, 2777–2788.
- (6) Elangovan, A.; Xu, J.; Brown, E.; Liu, B.; Li, J. Fundamental Electrochemical Insights of Vertically Aligned Carbon Nanofiber Architecture as a Catalyst Support for ORR. *J. Electrochem. Soc.* **2020**, *167*, 066523.
- (7) Bing, Y.; Liu, H.; Zhang, L.; Ghosh, D.; Zhang, J. Nanostructured Pt-Alloy Electrocatalysts for PEM Fuel Cell Oxygen Reduction Reaction. *Chem. Soc. Rev.* **2010**, *39*, 2184–2202.
- (8) Marković, N. M.; Schmidt, T. J.; Stamenković, V.; Ross, P. N. Oxygen Reduction Reaction on Pt and Pt Bimetallic Surfaces: A Selective Review. *Fuel Cells* **2001**, *1*, 105–116.
- (9) He, Y.; Liu, S.; Priest, C.; Shi, Q.; Wu, G. Atomically Dispersed Metal—Nitrogen—Carbon Catalysts for Fuel Cells: Advances in Catalyst Design, Electrode Performance, and Durability Improvement. *Chem. Soc. Rev.* **2020**, *49*, 3484—3524.
- (10) Zhu, Y.; Sokolowski, J.; Song, X.; He, Y.; Mei, Y.; Wu, G. Engineering Local Coordination Environments of Atomically Dispersed and Heteroatom-Coordinated Single Metal Site Electrocatalysts for Clean Energy-Conversion. *Adv. Energy Mater.* **2020**, *10*, 1902844.
- (11) Xu, J.; Liu, B. Intrinsic Properties of Nitrogen-Rich Carbon Nitride for Oxygen Reduction Reaction. *Appl. Surf. Sci.* **2020**, *500*, 144020.
- (12) Zhao, J.; Wang, W.; Qu, X.; Meng, Y.; Wu, Z. M-Porphyrin (M = Mn, Co) Carbon Materials as Oxygen Reduction Catalysts from Density Functional Studies. *Mol. Phys.* **2020**, *118*, No. e1687949.
- (13) Mun, Y.; Lee, S.; Kim, K.; Kim, S.; Lee, S.; Han, J. W.; Lee, J. Versatile Strategy for Tuning ORR Activity of a Single Fe-N4 Site by Controlling Electron-Withdrawing/Donating Properties of a Carbon Plane. J. Am. Chem. Soc. 2019, 141, 6254–6262.
- (14) Saputro, A. G.; Fajrial, A. K.; Maulana, A. L.; Fathurrahman, F.; Agusta, M. K.; Akbar, F. T.; Dipojono, H. K. Dissociative Oxygen Reduction Reaction Mechanism on the Neighboring Active Sites of a Boron-Doped Pyrolyzed Fe—N—C Catalyst. *J. Phys. Chem. C* **2020**, 124, 11383—11391.
- (15) Liu, K.; Wu, G.; Wang, G. Role of Local Carbon Structure Surrounding FeN4 Sites in Boosting the Catalytic Activity for Oxygen Reduction. *J. Phys. Chem. C* **2017**, *121*, 11319–11324.
- (16) Lee, D. H.; Lee, W. J.; Lee, W. J.; Kim, S. O.; Kim, Y.-H. Theory, Synthesis, and Oxygen Reduction Catalysis of Fe-Porphyrin-Like Carbon Nanotube. *Phys. Rev. Lett.* **2011**, *106*, 175502.
- (17) Liu, J.; Jiao, M.; Lu, L.; Barkholtz, H. M.; Li, Y.; Wang, Y.; Jiang, L.; Wu, Z.; Liu, D.; Zhuang, L.; et al. High Performance Platinum Single

- Atom Electrocatalyst for Oxygen Reduction Reaction. *Nat. Commun.* **2017**, *8*, 15938.
- (18) Yang, L.; Cheng, D.; Xu, H.; Zeng, X.; Wan, X.; Shui, J.; Xiang, Z.; Cao, D. Unveiling the High-Activity Origin of Single-Atom Iron Catalysts for Oxygen Reduction Reaction. *Proc. Natl. Acad. Sci. U.S.A.* **2018**, *115*, 6626–6631.
- (19) Zitolo, A.; Goellner, V.; Armel, V.; Sougrati, M.-T.; Mineva, T.; Stievano, L.; Fonda, E.; Jaouen, F. Identification of Catalytic Sites for Oxygen Reduction in Iron- and Nitrogen-Doped Graphene Materials. *Nat. Mater.* **2015**, *14*, 937–942.
- (20) Wu, G.; More, K. L.; Johnston, C. M.; Zelenay, P. High-Performance Electrocatalysts for Oxygen Reduction Derived from Polyaniline, Iron, and Cobalt. *Science* **2011**, 332, 443–447.
- (21) Hossen, M. M.; Artyushkova, K.; Atanassov, P.; Serov, A. Synthesis and Characterization of High Performing Fe-N-C Catalyst for Oxygen Reduction Reaction (ORR) in Alkaline Exchange Membrane Fuel Cells. *J. Power Sources* **2018**, *375*, 214–221.
- (22) Wang, M.; Yang, Y.; Liu, X.; Pu, Z.; Kou, Z.; Zhu, P.; Mu, S. The Role of Iron Nitrides in the Fe–N–C Catalysis System towards the Oxygen Reduction Reaction. *Nanoscale* **2017**, *9*, 7641–7649.
- (23) Jiang, W.-J.; Gu, L.; Li, L.; Zhang, Y.; Zhang, X.; Zhang, L.-J.; Wang, J.-Q.; Hu, J.-S.; Wei, Z.; Wan, L.-J. Understanding the High Activity of Fe–N–C Electrocatalysts in Oxygen Reduction: Fe/Fe₃C Nanoparticles Boost the Activity of Fe–Nx. *J. Am. Chem. Soc.* **2016**, 138, 3570–3578.
- (24) Martinez, U.; Holby, E. F.; Babu, S. K.; Artyushkova, K.; Lin, L.; Choudhury, S.; Purdy, G. M.; Zelenay, P. Experimental and Theoretical Trends of PGM-Free Electrocatalysts for the Oxygen Reduction Reaction with Different Transition Metals. *J. Electrochem. Soc.* **2019**, *166*, F3136–F3142.
- (25) Szakacs, C. E.; Lefèvre, M.; Kramm, U. I.; Dodelet, J.-P.; Vidal, F. A Density Functional Theory Study of Catalytic Sites for Oxygen Reduction in Fe/N/C Catalysts Used in $\rm H_2/O_2$ Fuel Cells. *Phys. Chem. Chem. Phys.* **2014**, *16*, 13654–13661.
- (26) Ma, T. Y.; Ran, J.; Dai, S.; Jaroniec, M.; Qiao, S. Z. Phosphorus-Doped Graphitic Carbon Nitrides Grown In Situ on Carbon-Fiber Paper: Flexible and Reversible Oxygen Electrodes. *Angew. Chem., Int. Ed.* **2015**, *54*, 4646–4650.
- (27) Yang, Y.; Zhang, H.; Liang, Z.; Yin, Y.; Mei, B.; Song, F.; Sun, F.; Gu, S.; Jiang, Z.; Wu, Y.; Zhu, Z. Role of Local Coordination in Bimetallic Sites for Oxygen Reduction: A Theoretical Analysis. *J. Energy Chem.* **2020**, *44*, 131–137.
- (28) Anderson, A. B.; Holby, E. F. Pathways for O_2 Electroreduction over Substitutional FeN₄, HOFeN₄, and OFeN₄ in Graphene Bulk Sites: Critical Evaluation of Overpotential Predictions Using LGER and CHE Models. *J. Phys. Chem. C* **2019**, *123*, 18398–18409.
- (29) Holby, E. F.; Zelenay, P. Linking Structure to Function: The Search for Active Sites in Non-Platinum Group Metal Oxygen Reduction Reaction Catalysts. *Nano Energy* **2016**, 29, 54–64.
- (30) Chung, H. T.; Cullen, D. A.; Higgins, D.; Sneed, B. T.; Holby, E. F.; More, K. L.; Zelenay, P. Direct Atomic-Level Insight into the Active Sites of a High-Performance PGM-Free ORR Catalyst. *Science* **2017**, 357, 479–484.
- (31) Han, Y.; Wang, Y.; Xu, R.; Chen, W.; Zheng, L.; Han, A.; Zhu, Y.; Zhang, J.; Zhang, H.; Luo, J.; et al. Electronic Structure Engineering to Boost Oxygen Reduction Activity by Controlling the Coordination of the Central Metal. *Energy Environ. Sci.* **2018**, *11*, 2348–2352.
- (32) Jia, Q.; Ramaswamy, N.; Hafiz, H.; Tylus, U.; Strickland, K.; Wu, G.; Barbiellini, B.; Bansil, A.; Holby, E. F.; Zelenay, P.; et al. Experimental Observation of Redox-Induced Fe–N Switching Behavior as a Determinant Role for Oxygen Reduction Activity. *ACS Nano* 2015, *9*, 12496–12505.
- (33) Zhu, H.; Paddison, S. J.; Zawodzinski, T. A. The Effects of the Ligand, Central Metal, and Solvent on the O₂ Binding of Non-Precious Metal Catalyst Model Systems: An Ab Initio Study. *Electrochim. Acta* **2013**, *101*, 293–300.
- (34) Holby, E. F.; Taylor, C. D. Activity of N-Coordinated Multi-Metal-Atom Active Site Structures for Pt-Free Oxygen Reduction Reaction Catalysis: Role of *OH Ligands. Sci. Rep. 2015, 5, 9286.

- (35) Cao, L.; Shao, Y.; Pan, H.; Lu, Z. Designing Efficient Dual-Metal Single-Atom Electrocatalyst TMZnN6 (TM = Mn, Fe, Co, Ni, Cu, Zn) for Oxygen Reduction Reaction. *J. Phys. Chem. C* **2020**, *124*, 11301–11307
- (36) Lu, Z.; Wang, B.; Hu, Y.; Liu, W.; Zhao, Y.; Yang, R.; Li, Z.; Luo, J.; Chi, B.; Jiang, Z.; et al. An Isolated Zinc—Cobalt Atomic Pair for Highly Active and Durable Oxygen Reduction. *Angew. Chem., Int. Ed.* **2019**, 58, 2622—2626.
- (37) Liu, D.; Wang, B.; Li, H.; Huang, S.; Liu, M.; Wang, J.; Wang, Q.; Zhang, J.; Zhao, Y. Distinguished Zn,Co-N_x-C-S_y Active Sites Confined in Dentric Carbon for Highly Efficient Oxygen Reduction Reaction and Flexible Zn-Air Batteries. *Nano Energy* **2019**, *58*, 277–283.
- (38) Chen, P.; Zhou, T.; Xing, L.; Xu, K.; Tong, Y.; Xie, H.; Zhang, L.; Yan, W.; Chu, W.; Wu, C.; Xie, Y. Atomically Dispersed Iron—Nitrogen Species as Electrocatalysts for Bifunctional Oxygen Evolution and Reduction Reactions. *Angew. Chem., Int. Ed.* **2017**, *56*, 610—614.
- (39) Wang, J.; Huang, Z.; Liu, W.; Chang, C.; Tang, H.; Li, Z.; Chen, W.; Jia, C.; Yao, T.; Wei, S.; et al. Design of N-Coordinated Dual-Metal Sites: A Stable and Active Pt-Free Catalyst for Acidic Oxygen Reduction Reaction. *J. Am. Chem. Soc.* **2017**, *139*, 17281–17284.
- (40) Zhang, D.; Chen, W.; Li, Z.; Chen, Y.; Zheng, L.; Gong, Y.; Li, Q.; Shen, R.; Han, Y.; Cheong, W.-C.; et al. Isolated Fe and Co Dual Active Sites on Nitrogen-Doped Carbon for a Highly Efficient Oxygen Reduction Reaction. *Chem. Commun.* **2018**, *54*, 4274–4277.
- (41) Wang, B.; Zou, J.; Shen, X.; Yang, Y.; Hu, G.; Li, W.; Peng, Z.; Banham, D.; Dong, A.; Zhao, D. Nanocrystal Supracrystal-Derived Atomically Dispersed Mn-Fe Catalysts with Enhanced Oxygen Reduction Activity. *Nano Energy* **2019**, *63*, 103851.
- (42) Holby, E. F.; Wu, G.; Zelenay, P.; Taylor, C. D. Structure of Fe—Nx—C Defects in Oxygen Reduction Reaction Catalysts from First-Principles Modeling. *J. Phys. Chem. C* **2014**, *118*, 14388–14393.
- (43) Zhang, L.; Fischer, J. M. T. A.; Jia, Y.; Yan, X.; Xu, W.; Wang, X.; Chen, J.; Yang, D.; Liu, H.; Zhuang, L.; et al. Coordination of Atomic Co–Pt Coupling Species at Carbon Defects as Active Sites for Oxygen Reduction Reaction. *J. Am. Chem. Soc.* **2018**, *140*, 10757–10763.
- (44) Wang, J.; Liu, W.; Luo, G.; Li, Z.; Zhao, C.; Zhang, H.; Zhu, M.; Xu, Q.; Wang, X.; Zhao, C.; et al. Synergistic Effect of Well-Defined Dual Sites Boosting the Oxygen Reduction Reaction. *Energy Environ. Sci.* **2018**, *11*, 3375–3379.
- (45) Chung, S.; Ham, K.; Kang, S.; Ju, H.; Lee, J. Enhanced Corrosion Tolerance and Highly Durable ORR Activity by Low Pt Electrocatalyst on Unique Pore Structured CNF in PEM Fuel Cell. *Electrochim. Acta* **2020**, 348, 136346.
- (46) Ge, X.; Sumboja, A.; Wuu, D.; An, T.; Li, B.; Goh, F. W. T.; Hor, T. S. A.; Zong, Y.; Liu, Z. Oxygen Reduction in Alkaline Media: From Mechanisms to Recent Advances of Catalysts. *ACS Catal.* **2015**, *5*, 4643–4667.
- (47) Hunter, M. A.; Fischer, J. M. T. A.; Yuan, Q.; Hankel, M.; Searles, D. J. Evaluating the Catalytic Efficiency of Paired, Single-Atom Catalysts for the Oxygen Reduction Reaction. *ACS Catal.* **2019**, *9*, 7660–7667.
- (48) Meng, Y.; Yin, C.; Li, K.; Tang, H.; Wang, Y.; Wu, Z. Improved Oxygen Reduction Activity in Heteronuclear FeCo-Codoped Graphene: A Theoretical Study. *ACS Sustainable Chem. Eng.* **2019**, 7, 17273–17281.
- (49) Kresse, G.; Furthmüller, J. Efficient Iterative Schemes for Ab Initio Total-Energy Calculations Using a Plane-Wave Basis Set. *Phys. Rev. B* **1996**, *54*, 11169–11186.
- (50) Kresse, G.; Furthmüller, J. Efficiency of Ab-Initio Total Energy Calculations for Metals and Semiconductors Using a Plane-Wave Basis Set. *Comput. Mater. Sci.* **1996**, *6*, 15–50.
- (51) Kresse, G.; Joubert, D. From Ultrasoft Pseudopotentials to the Projector Augmented-Wave Method. *Phys. Rev. B* **1999**, *59*, 1758–1775.
- (52) Perdew, J. P.; Burke, K.; Ernzerhof, M. Generalized Gradient Approximation Made Simple. *Phys. Rev. Lett.* **1996**, *77*, 3865–3868.
- (53) Monkhorst, H. J.; Pack, J. D. Special Points for Brillouin-Zone Integrations. *Phys. Rev. B* **1976**, *13*, 5188–5192.

- (54) Grimme, S.; Antony, J.; Ehrlich, S.; Krieg, H. A Consistent and Accurate Ab Initio Parametrization of Density Functional Dispersion Correction (DFT-D) for the 94 Elements H-Pu. *J. Chem. Phys.* **2010**, 132, 154104.
- (55) Kattel, S.; Wang, G. A Density Functional Theory Study of Oxygen Reduction Reaction on Me–N4 (Me = Fe, Co, or Ni) Clusters between Graphitic Pores. *J. Mater. Chem. A* **2013**, *1*, 10790–10797.
- (56) Nørskov, J. K.; Rossmeisl, J.; Logadottir, A.; Lindqvist, L.; Kitchin, J. R.; Bligaard, T.; Jónsson, H. Origin of the Overpotential for Oxygen Reduction at a Fuel-Cell Cathode. *J. Phys. Chem. B* **2004**, *108*, 17886–17892.
- (57) Zhao, S.; Wang, K.; Zou, X.; Gan, L.; Du, H.; Xu, C.; Kang, F.; Duan, W.; Li, J. Group VB Transition Metal Dichalcogenides for Oxygen Reduction Reaction and Strain-Enhanced Activity Governed by p-Orbital Electrons of Chalcogen. *Nano Res.* **2019**, *12*, 925–930.
- (58) Deng, Q.; Zhao, J.; Wu, T.; Chen, G.; Hansen, H. A.; Vegge, T. 2D Transition Metal—TCNQ Sheets as Bifunctional Single-Atom Catalysts for Oxygen Reduction and Evolution Reaction (ORR/OER). *J. Catal.* **2019**, *370*, *378*–384.
- (59) Dean, J. A. Lange's Handbook of Chemistry; McGraw-Hill: New York, 1985.
- (60) Ramaswamy, N.; Mukerjee, S. Fundamental Mechanistic Understanding of Electrocatalysis of Oxygen Reduction on Pt and Non-Pt Surfaces: Acid versus Alkaline Media. *Adv. Phys. Chem.* **2012**, 2012, 491604.
- (61) Choi, C. H.; Lim, H.-K.; Chung, M. W.; Park, J. C.; Shin, H.; Kim, H.; Woo, S. I. Long-Range Electron Transfer over Graphene-Based Catalyst for High-Performing Oxygen Reduction Reactions: Importance of Size, N-Doping, and Metallic Impurities. *J. Am. Chem. Soc.* **2014**, *136*, 9070–9077.
- (62) Anderson, A. B. Insights into Electrocatalysis. *Phys. Chem. Chem. Phys.* **2012**, *14*, 1330–1338.
- (63) Liu, S.; Cheng, L.; Wang, W.; Li, K.; Wang, Y.; Wu, Z. Fe-Porphyrin Carbon Matrix as a Bifunctional Catalyst for Oxygen Reduction and CO2 Reduction from Theoretical Perspective. *Mol. Phys.* **2019**, *117*, 1805–1812.
- (64) Nagaprasad Reddy, S.; Krishnamurthy, C. B.; Grinberg, I. First-Principles Study of the Ligand Substituent Effect on ORR Catalysis by Metallocorroles. *J. Phys. Chem. C* **2020**, *124*, 11275–11283.
- (65) Singh, K.; Razmjooei, F.; Yu, J.-S. Active Sites and Factors Influencing Them for Efficient Oxygen Reduction Reaction in Metal-N Coordinated Pyrolyzed and Non-Pyrolyzed Catalysts: A Review. *J. Mater. Chem. A* **2017**, *5*, 20095–20119.
- (66) Wang, Y.; Tang, Y.-J.; Zhou, K. Self-Adjusting Activity Induced by Intrinsic Reaction Intermediate in Fe-N-C Single-Atom Catalysts. *J. Am. Chem. Soc.* **2019**, *141*, 14115–14119.
- (67) Yang, X.; Xia, D.; Kang, Y.; Du, H.; Kang, F.; Gan, L.; Li, J. Unveiling the Axial Hydroxyl Ligand on Fe-N₄-C Electrocatalysts and Its Impact on the PH-Dependent Oxygen Reduction Activities and Poisoning Kinetics. *Adv. Sci.* **2020**, *7*, 2000176.
- (68) Chen, Y.; Ji, S.; Zhao, S.; Chen, W.; Dong, J.; Cheong, W.-C.; Shen, R.; Wen, X.; Zheng, L.; Rykov, A. I.; et al. Enhanced Oxygen Reduction with Single-Atomic-Site Iron Catalysts for a Zinc-Air Battery and Hydrogen-Air Fuel Cell. *Nat. Commun.* **2018**, *9*, 5422.
- (69) Greeley, J.; Stephens, I. E. L.; Bondarenko, A. S.; Johansson, T. P.; Hansen, H. A.; Jaramillo, T. F.; Rossmeisl, J.; Chorkendorff, I.; Nørskov, J. K. Alloys of Platinum and Early Transition Metals as Oxygen Reduction Electrocatalysts. *Nat. Chem.* **2009**, *1*, 552–556.
- (70) Kulkarni, A.; Siahrostami, S.; Patel, A.; Nørskov, J. K. Understanding Catalytic Activity Trends in the Oxygen Reduction Reaction. *Chem. Rev.* **2018**, *118*, 2302–2312.
- (71) Viswanathan, V.; Hansen, H. A.; Rossmeisl, J.; Nørskov, J. K. Universality in Oxygen Reduction Electrocatalysis on Metal Surfaces. *ACS Catal.* **2012**, *2*, 1654–1660.
- (72) Siahrostami, S.; Tsai, C.; Karamad, M.; Koitz, R.; García-Melchor, M.; Bajdich, M.; Vojvodic, A.; Abild-Pedersen, F.; Nørskov, J. K.; Studt, F. Two-Dimensional Materials as Catalysts for Energy Conversion. *Catal. Lett.* **2016**, *146*, 1917–1921.

- (73) Stephens, I. E. L.; Bondarenko, A. S.; Grønbjerg, U.; Rossmeisl, J.; Chorkendorff, I. Understanding the Electrocatalysis of Oxygen Reduction on Platinum and Its Alloys. *Energy Environ. Sci.* **2012**, *5*, 6744–6762.
- (74) Liu, F.; Zhu, G.; Yang, D.; Jia, D.; Jin, F.; Wang, W. Systematic Exploration of N, C Configurational Effects on the ORR Performance of Fe–N Doped Graphene Catalysts Based on DFT Calculations. RSC Adv. 2019, 9, 22656–22667.